IEEE Access
Multidisciplinary ⋮ Rapid Review ⋮ Open Access Journal

Received February 8, 2019, accepted April 1, 2019, date of publication April 11, 2019, date of current version April 23, 2019.

*Digital Object Identifier 10.1109/ACCESS.2019.2909973*

# Design and Experiment of Dual-Mass MEMS Gyroscope Sense Closed System Based on Bipole Compensation Method

**HUILIANG CAO, (Member, IEEE), YU LIU, YINGJIE ZHANG, XINGLING SHAO, JINYANG GAO, KUN HUANG, YUNBO SHI, JUN TANG, CHONG SHEN, AND JUN LIU**

Science and Technology on Electronic Test and Measurement Laboratory, North University of China, Taiyuan 030051, China

Corresponding authors: Chong Shen (shenchong@nuc.edu.cn) and Jun Liu (liuj@nuc.edu.cn)

This work was supported in part by the National Natural Science Foundation of China under Grant 51705477, Grant 61603353, Grant 61803347, and Grant 61703098, in part by the Pre-Research Field Foundation of Equipment Development Department of China under Grant 61405170104, in part by the Program for the Top Young Academic Leaders of Higher Learning Institutions of Shanxi, in part by the Fund Program for the Scientific Activities of Selected Returned Overseas Professionals in Shanxi Province, in part by the Shanxi Province Science Foundation for Youths under Grant 201801D221195, in part by the Young Academic Leaders of the North University of China under Grant QX201809, in part by the Fund of Science and Technology on Electronic Test and Measurement Laboratory under Grant WD614200104011804, in part by the Open Fund of the State Key Laboratory of Deep Buried Target Damage under Grant DXMBJJ2017-15 and Grant DXMBJJ2018-07, and in part by the Fund for Shanxi 1331 Project Key Subjects Construction.

**ABSTRACT** This paper presents a sense mode closed-loop method for dual-mass micro-electro-mechanical system (MEMS) gyroscope based on the bipole temperature compensation method. A pair of conjugate poles are investigated as the bottle neck of the sense closed-loop system of MEMS gyroscope, and the bipole temperature compensation proportional controller (BTCPC) is employed to realize the closed-loop: a pair of additional conjugate zeros are utilized to generate bipoles with poles. Since poles changes with temperature, thermal resistance is utilized in BTCPC to make zeros variable with temperatures. The BTCPC is designed very carefully to make the system have enough bandwidth and better performance. The overall gyroscope model is established and simulated either in the time domain or the frequency domain, and the results verify that the sense closed-loop works rapidly and steadily. The system is realized on PCBs and is tested on the turntable in temperature oven. The experimental results show that the bias stability, angular random walking, bias temperature coefficient, and the bandwidth values of sense open-loop and closed-loop are 2.168 °/h, 0.155 °/$\sqrt{}$h, 9.534 °/h/°C, 13 Hz, and 2.168 °/h, 0.140 °/$\sqrt{}$h (five tests average value), 5.991 °/h°C, 61 Hz, respectively.

**INDEX TERMS** Dual-mass MEMS gyroscope, bipole-temperature compensation controller, experiment, sense closed-loop.

## I. INTRODUCTION

The MEMS gyroscopes and devices are utilized in more and more application areas, including automotive safety, energy harvesting, industrial controlling, inertial navigation, and consumer electronics [1]–[3]. A lot of work are reported to improve the gyro characteristic, including bias drift prediction [4], tiny capacitance detection interface circuit [5], structure noising analysis [6], quality factor optimization [7], structure advanced manufacture [8], bandwidth expanding [9], [10], data compensation [11]–[13], quadrature error correction [14], and so on. For most linear vibrating MEMS gyroscopes structure, the mechanical sensitivity and mechanical bandwidth are both governed by the resonant frequency split of drive and sense modes' $\Delta f$ [9]. Sense mode closed-loop technology is employed to improve the precision of MEMS gyro. The sensing closed-loop for single mass MEMS gyroscope based on automatic gain control (AGC) technology is proposed in paper [15]. Another sensing mode closed-loop was reported in work [16], in this work, a simple PI controller was utilized, and the results were outstanding (bias stability was

The associate editor coordinating the review of this manuscript and approving it for publication was Hadi Heidari.

about 3 °/h) during a wide temperature range. The notch filter was employed in sense closed-loop in work [17], and the experiments show that the bandwidth, nonlinearity and scale factor temperature coefficient were optimized after sense loop was closed. PI controller were employed in sense closed-loop in work [18] and [19], and the characteristic of MEMS gyroscopes were improved obviously. The work in [20], [21] and [22] employed genetic algorithm and Σ-Δ modulator in sense closed-loop, and 6th order band-pass modulator was reported. A novel model predictive control method was utilized in sense closed-loop in work [23]. In work [24], a novel narrow-band force rebalance control method for the sense mode of MEMS gyroscope was presented, and a band pass filter was utilized to substitute the demodulation and modulation module. Work [25] proposed a novel robust design method for the sense closed-loop based on fuzzy reliability and Taguchi design, the method enhanced the temperature characteristic obviously. A novel decentralized force-to-rebalance closed-loop control method was proposed in [26], and the bias stability of the MEMS gyroscope improves obviously. Work [27] reported a controllable MEMS gyroscope design concept with the help of a new 2-degreesof-freedom (2-DOF) sense mode oscillator to linearize the electrostatic control force.

The work in this paper focuses on the sense mode closed-loop design and experiment. And the goal of the loop is supposed to improve the MEMS gyroscope characteristic in the following aspects: bias stability, bandwidth, temperature coefficient and scale factor nonlinearity. This paper is organized as following: Section II introduces the dual-mass sensing mode coupling MEMS gyroscope structure. In Section III, sense closed-loop method based on bipole temperature compensation proportional controller (BTCPC) are described, including the controller and system design and simulation. Then, the gyroscope monitoring system and experimental results based on BTCPC are given in Section IV. The results discussion and concluding remarks are shown in Section V.

## II. DUAL-MESS MEMS GYROSCOPE STRUCTURE

The dual-mass sensing mode coupling MEMS gyroscope structure researched in this paper is shown in figure 1 [6].

This architecture is constituted by two symmetrical parts, which are connected by two center U-shaped connect springs whose parameters are same with drive U-shaped spring. The left and right Coriolis mass are sustained by 2 drive U-shaped springs (DS-A, B) and 4 sense U-shaped springs (SS-C, D, E, F) respectively, and these springs linked by drive and sense frames. The moving comb fingers combined with frames while the static ones fixed with the substrate. The whole architecture is suspended and supported by 8 drive (DS-C, D, E, F for left part) and 4 sense (SS-A, B) U-shaped springs. Turning fork theory is employed in drive mode, the left and right masses are connected and coupled by connect U-shaped spring, when two sensing masses are coupled by the $x$ axis warp of drive springs.

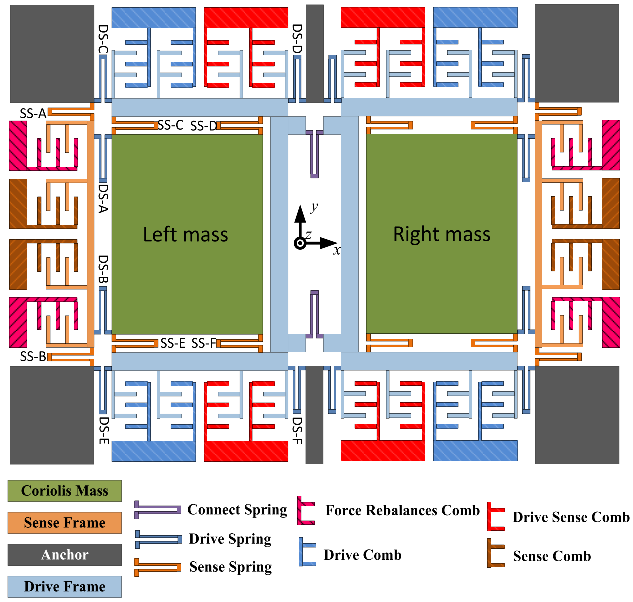


**FIGURE 1. The dual-mass sensing mode coupling MEMS gyroscope structure schematic.**

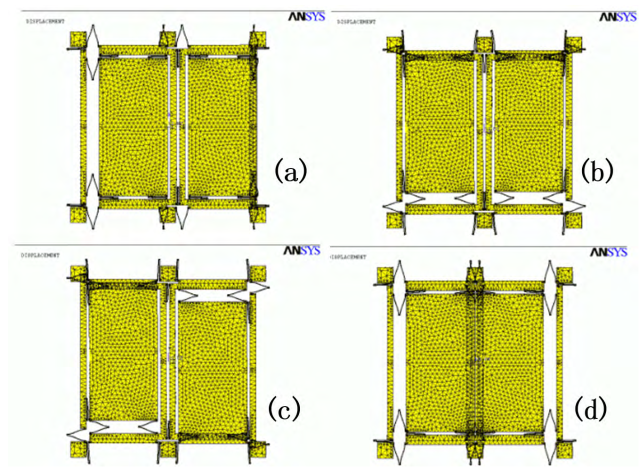


**FIGURE 2. The first four orders modes of dual-mass sensing mode coupling MEMS gyroscope structure: (a) Drive in phase mode (first mode) with frequency $\omega_{x1} = 2623 \times 2\pi$ rad/s; (b) Sensing in phase mode (second mode) with frequency $\omega_{y1} = 3342 \times 2\pi$ rad/s; (c) Sensing anti phase mode (third mode) with frequency $\omega_{y2} = 3468 \times 2\pi$ rad/s; (d) Drive anti phase mode (fourth mode) with frequency $\omega_{x2} = 3484 \times 2\pi$ rad/s.**

The first four order modes of the structure are analyzed and shown in figure 2:

Fig. 2 (a) shows the 1st mode, the drive in-phase mode, left and right masses move in same direction along $x$ axis.

Fig. 2 (b) shows the 2nd mode, the sensing in-phase mode, left and right masses move in same direction along $y$ axis.

Fig. 2 (c) shows the 3rd mode, sensing anti-phase mode, left and right masses move in inverse direction along $y$ axis.

Fig. 2 (d), shows the 4th mode, drive anti-phase mode, left and right masses move in inverse direction along $x$ axis.

The drive anti-phase is expected drive mode. So, left and right Coriolis masses both have two degrees of freedom (along x and y axis). Drive frame has one degrees of freedom (along x axis) and sense frame has one degrees of freedom (along y axis). The angular input axis is z axis in figure 1. The real working sensing mode is proved as the superposition of 2nd and 3rd modes, and the motion equation is [9]:

$$\boldsymbol{m}\ddot{\boldsymbol{D}} + \boldsymbol{\omega}\boldsymbol{m}\frac{\mathbf{1}}{\boldsymbol{f}\boldsymbol{Q}}\dot{\boldsymbol{D}} + \boldsymbol{m}\boldsymbol{\omega}^2\boldsymbol{D} = \boldsymbol{F} \tag{1}$$

where,

$$\boldsymbol{m} = \begin{bmatrix} m_x & 0 & 0 \\ 0 & m_y & 0 \\ 0 & 0 & m_y \end{bmatrix}, \quad \boldsymbol{D} = \begin{bmatrix} x \\ y_1 \\ y_2 \end{bmatrix},$$

$$\frac{1}{\boldsymbol{Q}} = \begin{bmatrix} \frac{1}{Q_{x2}} & 0 & 0 \\ 0 & \frac{1}{Q_{y1}} & 0 \\ 0 & 0 & \frac{1}{Q_{y2}} \end{bmatrix},$$

$$\boldsymbol{\omega} = \begin{bmatrix} \omega_{x2} & 0 & 0 \\ 0 & \omega_{y1} & 0 \\ 0 & 0 & \omega_{y2} \end{bmatrix}, \quad \boldsymbol{F} = \begin{bmatrix} F_{drive} \\ -2m_c\Omega_z\dot{x} + F_{yfc} \\ -2m_c\Omega_z\dot{x} + F_{yfc} \end{bmatrix}$$

are the mass, displacement, quality factor, resonant frequency, and external force matrix respectively; $m_x$ is drive mode equivalent mass; $x$ and $Q_{x2}$ are drive (anti-phase) mode displacement and quality factor; $y_1$, $y_2$, $Q_{y1}$ and $Q_{y2}$ are sense in-phase and anti-phase mode displacements and quality factors; $\Omega_z$ is angular rate input; sense mode mass $m_y$ approximates to Coriolis mass $m_c$; drive mode electrostatic force $F_{drive} = F_d sin\omega_d t)$, $F_d$ and $\omega_d$ are drive mode stimulating magnitude and frequency; $F_{yfc}$ is sense mode feedback force, and in the beginning, it is set as 0 to achieve sense mode displacement characteristic $y = y_1 + y_2$, and we get (2) and (3), as shown at the bottom of this page.

## III. SENSE CLOSED-LOOP DESIGN

### A. SENSE CLOSED-LOOP ANALYSIS

The dual-mass MEMS gyroscope sense closed-loop system schematic is shown in figure 3.

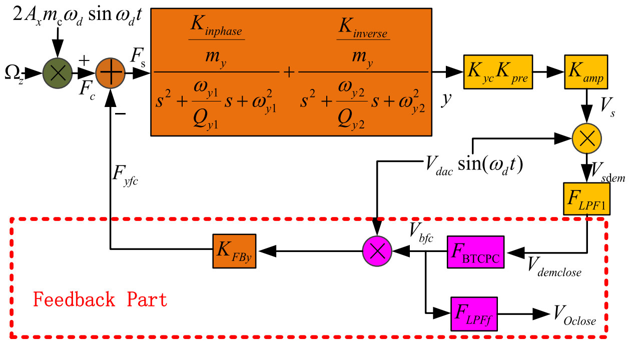


**FIGURE 3. The dual-mass MEMS gyroscope sense closed-loop system schematic.**

In figure 3, it can be seen that the structure is dual-mass and sensing mode coupling structure, and the sense mode is the superposition of sense in-phase mode and sense anti-phase mode [9]. $K_{yc}$ and $K_{pre}$ are displacement to capacitance transform function and pre-amplifier; $K_{amp}$ is second differential amplifier; $F_{LPF1}$ is second order low pass filter, $F_{BTCPC}$ is the controller; $K_{FBy}$ is voltage-force interface transform coefficient of force rebalances combs; $K_{inphase}$ and $K_{inverse}$ are displace-voltage transform parameters of sensing in-phase and anti-phase modes and $K_{inverse} \gg K_{inphase}$, and the following equations can be get:

$$F_c(t) = 2\Omega_z(t)\, m_y A_x \omega_d \sin(\omega_d t) \tag{4}$$

$$F_{\text{yfc}}(t) = K_{\text{FBy}} V_{\text{bfc}}(t)\, V_{\text{dac}} \sin(\omega_d t) \tag{5}$$

$$F_{\text{s}}(t) = F_c(t) - F_{\text{yfc}}(t) \tag{6}$$

$$V_{\text{sdem}}(t) = V_s(t)\, V_{dac} \sin(\omega_d t) \tag{7}$$

$$V_{\text{bfc}}(t) = V_{\text{sdem}} F_{LPF1} F_{\text{BTCPC}} \tag{8}$$

$$V_{Oclose} = V_{\text{bfc}}(t)\, F_{LPFf} \tag{9}$$

Substituting Equations (4) and (5) into (6), and after Laplace transformation, it can be get that:

$$\begin{aligned} F_{\text{s}}(\text{s}) &= 2m_y A_x \omega_d (\Omega_z(s - j\omega_d) + \Omega_z(s + j\omega_d)) \\ &\quad - K_{\text{FBy}} V_{\text{dac}} (V_{\text{bfc}}(s - j\omega_d) + V_{\text{bfc}}(s + j\omega_d)) \end{aligned} \tag{10}$$

$$\begin{aligned} x(t) &= \frac{F_d \sin(\omega_d t - tg^{-1}\left(\frac{\omega_{x2}\omega_d}{Q_{x2}(\omega_{x2}^2 - \omega_d^2)}\right))}{m_x\sqrt{\left(\omega_{x2}^2 - \omega_d^2\right)^2 + \omega_{x2}^2\omega_d^2/Q_{x2}^2}} \\ \xrightarrow{\omega_d = \omega_{x2}} x(t) &= \frac{F_d Q_{x2}}{m_x \omega_d^2}\cos(\omega_d t) = A_x \cos(\omega_d t) \end{aligned} \tag{2}$$

$$\begin{aligned} y_{1,2}(t) &= -2\Omega_z\omega_d F_d \cdot \frac{\sin(\omega_d t - tg^{-1}\left(\frac{\omega_{x2}\omega_d}{Q_{x2}(\omega_{x2}^2 - \omega_d^2)}\right) + \frac{\pi}{2} - tg^{-1}\left(\frac{\omega_{y1,2}\omega_d}{Q_{y1,2}(\omega_{y1,2}^2 - \omega_d^2)}\right))}{m_x\sqrt{\left(\omega_{x2}^2 - \omega_d^2\right)^2 + \omega_{x2}^2\omega_d^2/Q_{x2}^2}\sqrt{\left(\omega_{y1,2}^2 - \omega_d^2\right)^2 + \omega_{y1,2}^2\omega_d^2/Q_{y1,2}^2}} \\ \xrightarrow{\omega_d = \omega_{x2}} y_{1,2}(t) &= \frac{-2\Omega_z F_d Q_{x2}\sin(\omega_d t)}{m_x\omega_d\sqrt{\left(\omega_{y1,2}^2 - \omega_d^2\right)^2 + \omega_{y1,2}^2\omega_d^2/Q_{y1,2}^2}} \\ &= A_{y1,2}\sin(\omega_d t) \end{aligned} \tag{3}$$

Then

$$V_s(s) = K_{yc}K_{pre}K_{amp} \cdot \left[2m_y A_x \omega_d(\Omega_z(s-j\omega_d)+\Omega_z(s+j\omega_d)) - K_{\mathrm{FBy}}V_{\mathrm{dac}}(V_{\mathrm{bfc}}(s-j\omega_d)+V_{\mathrm{bfc}}(s+j\omega_d))\right] \cdot \left(\frac{K_{inphase}}{s^2+\frac{\omega_{y1}}{Q_{y1}}s+\omega_{y1}^2}+\frac{K_{inverse}}{s^2+\frac{\omega_{y2}}{Q_{y2}}s+\omega_{y2}^2}\right) \quad (11)$$

And after Equation (7) Laplace transformation, substituting Equation (11) into it, then (12), as shown at the bottom of this page. The low pass filter $F_{LPF1}$ cut off the high frequency components, then, the output of the sense closed-loop $V_{Oclose}$ can be expressed as:

$$\frac{V_{\mathrm{Oclose}}(s)}{\Omega_z(s)} = \frac{2K_{yc}K_{pre}K_{amp}V_{dac}F_{LPF1}F_{\mathrm{BTCPC}}F_{LPFf}m_yA_x\omega_dG_{sE}}{4m_y+K_{yc}K_{pre}K_{amp}V_{dac}^2F_{LPF1}F_{\mathrm{BTCPC}}K_{\mathrm{FBy}}G_{sE}} \quad (13)$$

where

$$G_{sE} = \left\{\frac{K_{inphase}(s^2+\frac{\omega_{y1}}{Q_{y1}}s+\omega_{y1}^2-\omega_d^2)}{(s^2+\frac{\omega_{y1}}{Q_{y1}}s+\omega_{y1}^2-\omega_d^2)^2+(2s\omega_d+\frac{\omega_{y1}}{Q_{y1}}\omega_d)^2} + \frac{K_{inverse}(s^2+\frac{\omega_{y2}}{Q_{y2}}s+\omega_{y2}^2-\omega_d^2)}{(s^2+\frac{\omega_{y2}}{Q_{y2}}s+\omega_{y2}^2-\omega_d^2)^2+(2s\omega_d+\frac{\omega_{y2}}{Q_{y2}}\omega_d)^2}\right\}$$

And, the poles of $G_{sE}$ are:

$$p_{1,2} = -\frac{\omega_{y2}}{2Q_{y2}} \pm (\omega_{x2}-\frac{\omega_{y2}}{2}\sqrt{4-\frac{1}{Q_{y2}^2}})j$$
$$p_{3,4} = -\frac{\omega_{y1}}{2Q_{y1}} \pm (\omega_{x2}-\frac{\omega_{y1}}{2}\sqrt{4-\frac{1}{Q_{y1}^2}})j$$
$$p_{5,6} = -\frac{\omega_{y2}}{2Q_{y2}} \pm (\omega_{x2}+\frac{\omega_{y2}}{2}\sqrt{4-\frac{1}{Q_{y2}^2}})j$$
$$p_{7,8} = -\frac{\omega_{y1}}{2Q_{y1}} \pm (\omega_{x2}+\frac{\omega_{y1}}{2}\sqrt{4-\frac{1}{Q_{y1}^2}})j$$

When $4m_y \gg K_{yc}K_{pre}K_{amp}V_{dac}^2F_{LPF1}F_{\mathrm{BTCPC}}K_{\mathrm{FBy}}G_{sE}$, and:

$$\left|\frac{V_{\mathrm{Oclose}}(s)}{\Omega_z(s)}\right| = \frac{K_{yc}K_{pre}K_{amp}V_{dac}F_{LPF1}F_{\mathrm{BTCPC}}F_{LPFf}A_x\omega_dG_{sE}}{2} \quad (14)$$

### B. BTCPC DESIGN AND SIMULATION

The dual-mass MEMS gyroscope sense open-loop system (remove the "Feedback Part" in Figure 3) bode map is shown in figure 4. The "peak" is generated by $p_{1,2}$ at frequency $\omega_2$ (resonant frequency split of $\omega_{x2}$ and $\omega_{y2}$). Since the resonant frequencies and quality factors of drive and sense mode move with temperature, the bode map is simulated under different temperatures. It is obviously that the conjugate poles $p_{1,2}$ limited the phase and amplitude margin of the system, and the value changes with temperature. Then, the BTCPC is designed with following requirement:

① BTCPC should generate a pair of conjugate zeros (named as $z_{c1}$ and $z_{c2}$) to compensate the influence of poles $p_1$, and $p_2$. Then, the transfer function of BTCPC can be

$$V_{\mathrm{sdem}}(s) = \frac{K_{yc}K_{pre}K_{amp}V_{dac}}{2} \cdot \left(\begin{array}{l} 2m_yA_x\omega_d \\ \cdot\left\{\left(\frac{[\Omega_z(s)+\Omega_z(s+2j\omega_d)]K_{inphase}}{(s+j\omega_d)^2+\frac{\omega_{y1}}{Q_{y1}}(s+j\omega_d)+\omega_{y1}^2}+\frac{[\Omega_z(s)+\Omega_z(s+2j\omega_d)]K_{inverse}}{(s+j\omega_d)^2+\frac{\omega_{y2}}{Q_{y2}}(s+j\omega_d)+\omega_{y2}^2}\right) + \left(\frac{[\Omega_z(s-2j\omega_d)+\Omega_z(s)]K_{inphase}}{(s-j\omega_d)^2+\frac{\omega_{y1}}{Q_{y1}}(s-j\omega_d)+\omega_{y1}^2}+\frac{[\Omega_z(s-2j\omega_d)+\Omega_z(s)]K_{inverse}}{(s-j\omega_d)^2+\frac{\omega_{y2}}{Q_{y2}}(s-j\omega_d)+\omega_{y2}^2}\right)\right\} \\ -K_{\mathrm{FBy}}V_{\mathrm{dac}} \\ \cdot\left\{\left(\frac{[V_{\mathrm{bfc}}(s)+V_{\mathrm{bfc}}(s+2j\omega_d)]K_{inphase}}{(s+j\omega_d)^2+\frac{\omega_{y1}}{Q_{y1}}(s+j\omega_d)+\omega_{y1}^2}+\frac{[V_{\mathrm{bfc}}(s)+V_{\mathrm{bfc}}(s+2j\omega_d)]K_{inverse}}{(s+j\omega_d)^2+\frac{\omega_{y2}}{Q_{y2}}(s+j\omega_d)+\omega_{y2}^2}\right) + \left(\frac{[V_{\mathrm{bfc}}(s-2j\omega_d)+V_{\mathrm{bfc}}(s)]K_{inphase}}{(s-j\omega_d)^2+\frac{\omega_{y1}}{Q_{y1}}(s-j\omega_d)+\omega_{y1}^2}+\frac{[V_{\mathrm{bfc}}(s-2j\omega_d)+V_{\mathrm{bfc}}(s)]K_{inverse}}{(s-j\omega_d)^2+\frac{\omega_{y2}}{Q_{y2}}(s-j\omega_d)+\omega_{y2}^2}\right)\right\} \end{array}\right) \quad (12)$$

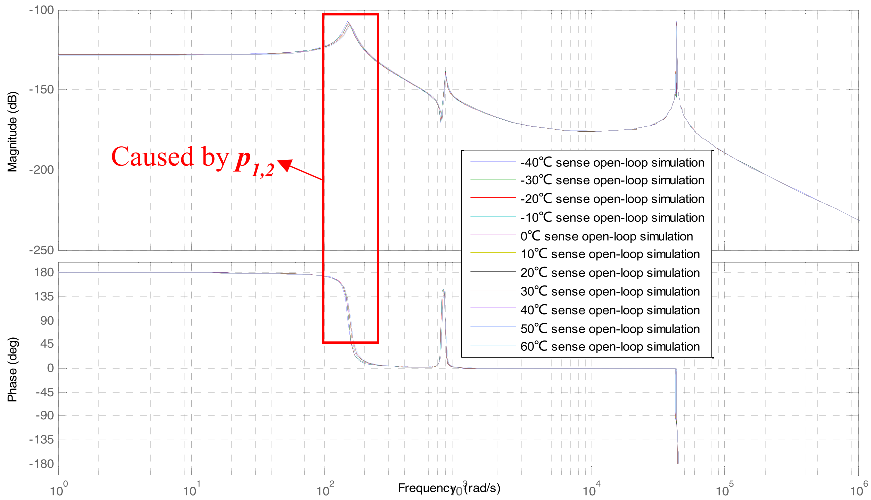


**FIGURE 4.** The MEMS gyroscope sense open-loop bode map.

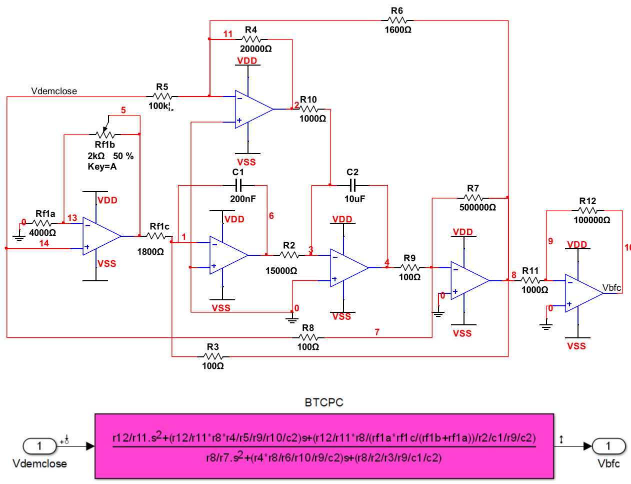


**FIGURE 5.** BTCPC circuit and system level models.

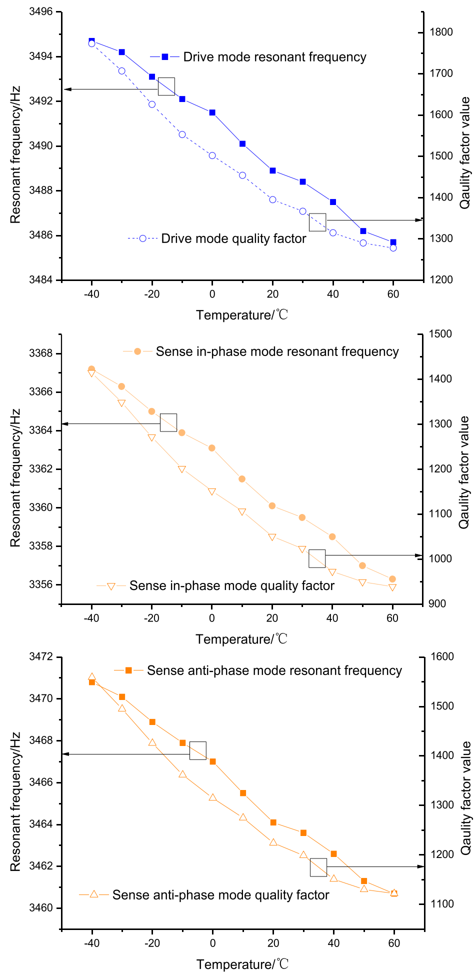


**FIGURE 6.** MEMS gyroscope structure mechanical parameters.

expressed as:

$$F_{\mathrm{BTCPC}} = \frac{(s\text{-}z_{c1})\,(s\text{-}z_{c2})}{A_{\mathrm{BTCPC}}\,(s+\omega_{\mathrm{BTCPC}})^2} = \frac{\left[\begin{array}{c}\left(s+\frac{\omega_{y2}}{2Q_{y2}}+(\omega_{x2}-\frac{\omega_{y2}}{2}\sqrt{4-\frac{1}{Q_{y2}^2}})j\right)\\ \cdot\left(s+\frac{\omega_{y2}}{2Q_{y2}}-(\omega_{x2}-\frac{\omega_{y2}}{2}\sqrt{4-\frac{1}{Q_{y2}^2}})j\right)\end{array}\right]}{A_{\mathrm{BTCPC}}\,(s+\omega_{\mathrm{BTCPC}})^2} \tag{15}$$

where, $A_{BTCPC}$ is the reciprocal of gain (proportional component), $\omega_{BTCPC}$ is the pole of BTCPC. And, in this work, the gyroscope structure is in vacuum package and $Q_{y2} > 2000$, and then the above equation can be simplified as:

$$F_{\mathrm{BTCPC}} = \frac{1}{A_{\mathrm{BTCPC}}}\frac{s^2+\frac{\omega_{y2}}{Q_{y2}}s+\Delta\omega_2^2}{s^2+2\omega_{\mathrm{BTCPC}}s+\omega_{\mathrm{BTCPC}}^2} \tag{16}$$

② The BTCPC can expanding the bandwidth of the gyroscope, and the bandwidth is supposed to more than 50 Hz. So, the pole of BTCPC $\omega_{BTCPC}$ should be designed as more than 314 ($50\times 2\pi$) rad/s.

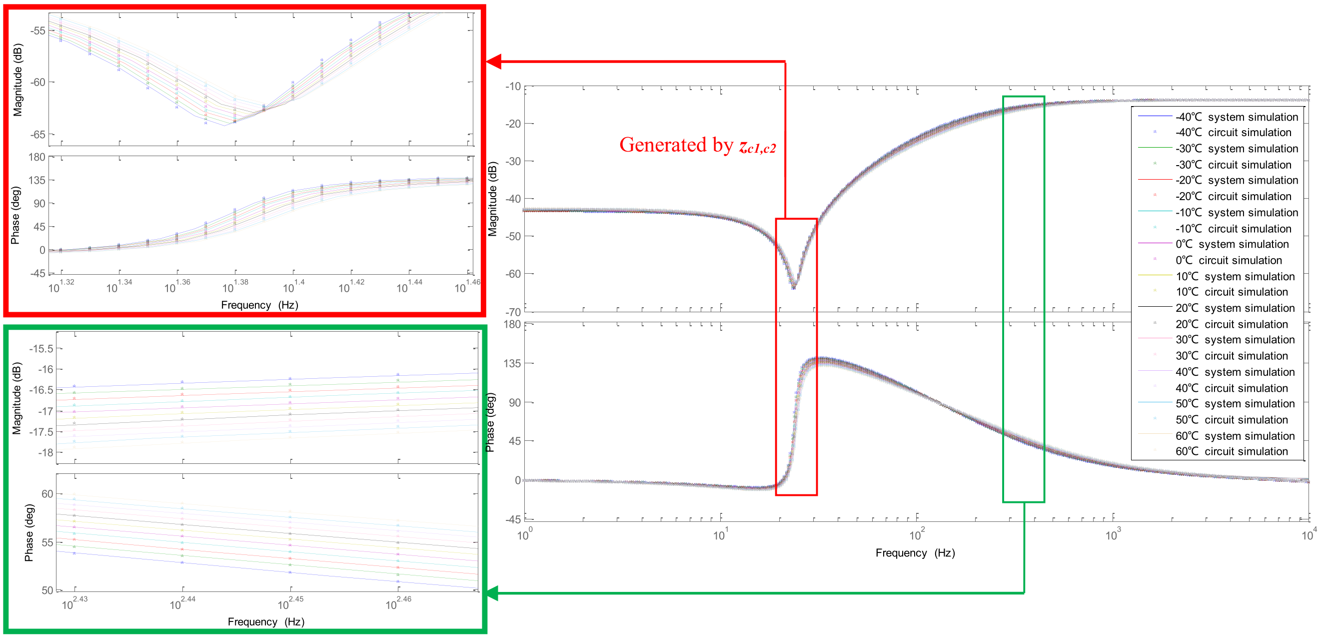


**FIGURE 7.** BPCTC circuit and system level simulation under different temperatures.

③ The gain of the BTCPC is not suitable to be too large, otherwise the system will be unstable, and this paper makes this value is adjustable.

④ Since poles $p_1$, and $p_2$ verify with temperature, $z_{c1}$ and $z_{c2}$ should be changed with the temperature.

⑤ The poles of BTCPC are designed as two-same real root to avoid the influence of "peak" generated by imaginary roots, and the magnitude frequency curve decays rapidly at a slope of −40dB outside the bandwidth.

After the analysis of the requirement of BTCPC, the circuit together with the parameters is proposed in the figure 5. And transfer function can be expressed as:

$$F_{\mathrm{BTCPC}} = \frac{V_{\mathrm{bfc}}}{V_{\mathrm{demclose}}} = \frac{R_{12}R_7}{R_{11}R_8}\frac{s^2 + \frac{R_8R_4}{R_5R_9R_{10}C_2}s + \frac{R_8}{R_1R_2R_9C_1C_2}}{s^2 + \frac{R_4R_7}{R_6R_9R_{10}C_2}s + \frac{R_7}{R_2R_3R_9C_1C_2}} \quad (17)$$

In order to satisfy the design rule ④, this paper employs a thermal resistance, and the resistance $R_1$ is divided as three resistances: $R_1 = \frac{R_{f1a}R_{f1c}}{R_{f1b}+R_{f1a}}$, and make $R_{f1b} \gg R_{fab}$, then $R_1 = \frac{R_{f1a}R_{f1c}}{R_{f1b}}$, and $R_{f1b}$ is the thermal resistance, it value is:

$$R_{f1b} = 1000 + 3.9T \quad (18)$$

where, $T$ is the temperature centigrade degree. This paper analyzed the BTCPC in both circuit level and system level with different mechanical parameters (resonant frequency and quality factor) under different temperatures (from −40°C to 60°C). The mechanical parameters vs temperature curves are shown in figure 6 (the trend follow same direction and the resonant frequencies change about 0.3%, while quality factors change more than 20%). And the circuit and system level simulation curves are shown in figure 7.

From figure 7, it is obviously that the compensation zeros of BPCTC generate a "valley" at about 24 Hz which is the value of $\omega_2$, and matches the "peak" in figure 4. And the simulation results verify the function of BPCTC. Meanwhile, the circuit level simulation results match the system level simulation results, which proves the circuit can satisfy the requirement of BPCTC module in system.

### C. MEMS GYROSCOPE SENSE CLOSED-LOOP SYSTEM REALIZATION AND SIMULATION

The dual-mass MEMS gyroscope sense closed-loop system schematic is shown in figure 8. In drive loop, drive mode displacement $x(t)$ is detected by drive sense combs and processed by differential amplifier ①. Then, module ② delays the signal phase with 90° to satisfy the phase requirement of AC drive signal $V_{dac}Sin(\omega_d t)$. After that, full-wave rectifier ③ and a low pass filter ④ pick up the amplitude of $V_{dac}Sin(\omega_d t)$. And, $V_{dac}$ is compared with the reference voltage $V_{ref}$ ⑥ through module ⑤. Next, drive closed loop PI controller ⑦ generates the control signal, which is modulated by $V_{dac}Sin(\omega_d t)$, and then the signal is superposed (through ⑩) by $V_{DC}$ ⑨ to stimulation drive mode.

The sense loop utilizes a similar interface. Firstly, the left and right Coriolis masses' movement signals are detected separately with differential detection amplifiers ⑪. And the output signals are processed by second differential amplifier ⑫ to form sense mode movement signal $V_{stotal}$.

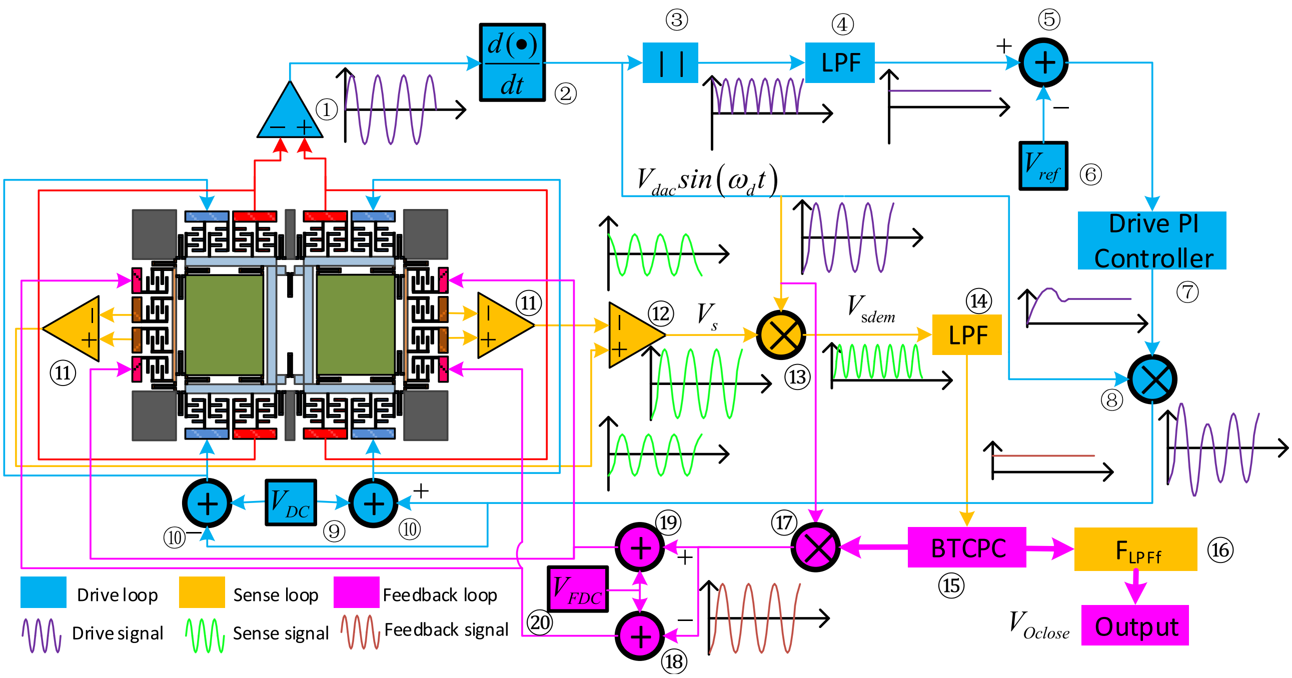


**FIGURE 8.** MEMS gyroscope monitoring system schematic.

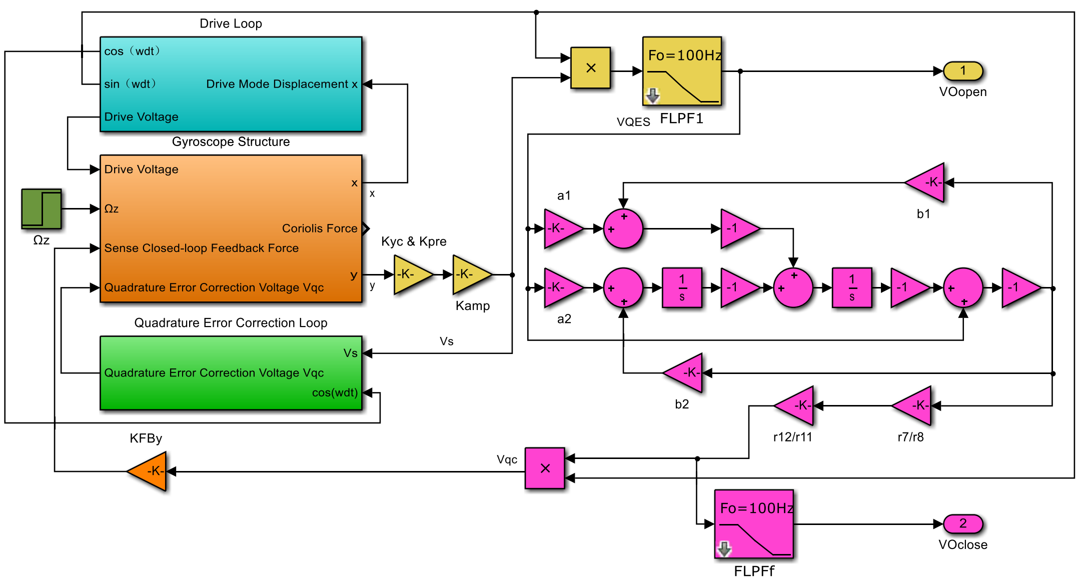


**FIGURE 9.** The MEMS gyroscope system modal in Simulink Soft.

Then, $V_{stotal}$ is demodulated by signal $V_{dac}Sin(\omega_d t)$ (in ⑬) and demodulated signal $V_{dem}$ is generated. After that, $V_{dem}$ passes through the low pass filter ⑭ and forms the sense open loop signal $V_{Oopen}$. For sense feedback loop, $V_{Oopen}$ is first sent in BTCPC ⑮ to calculate the control signal superposed (through ⑯) with test signal $V_{Tes}$ ⑰. Then the signal is modulated with $V_{dac}Sin(\omega_d t)$ (in ⑱) to form the AC feedback signal. Finally, DC voltage $V_{FDC}$ ⑳ is superposed with the AC feedback signal in ⑲ to generate the feedback signal. The output level low pass filter "$F_{LPFf}$" is configured to satisfy the different bandwidth requirements of the customers.

The dual-mass MEMS gyroscope sense closed-loop system modal is established in Simulink Soft and is shown in Figure. 9. The model contains five part: the gyroscope structure part (orange color), the drive loop part (cyan color), the quadrature error part (green color, and this part is reported in [14] and is separated from sense channel, so it did not

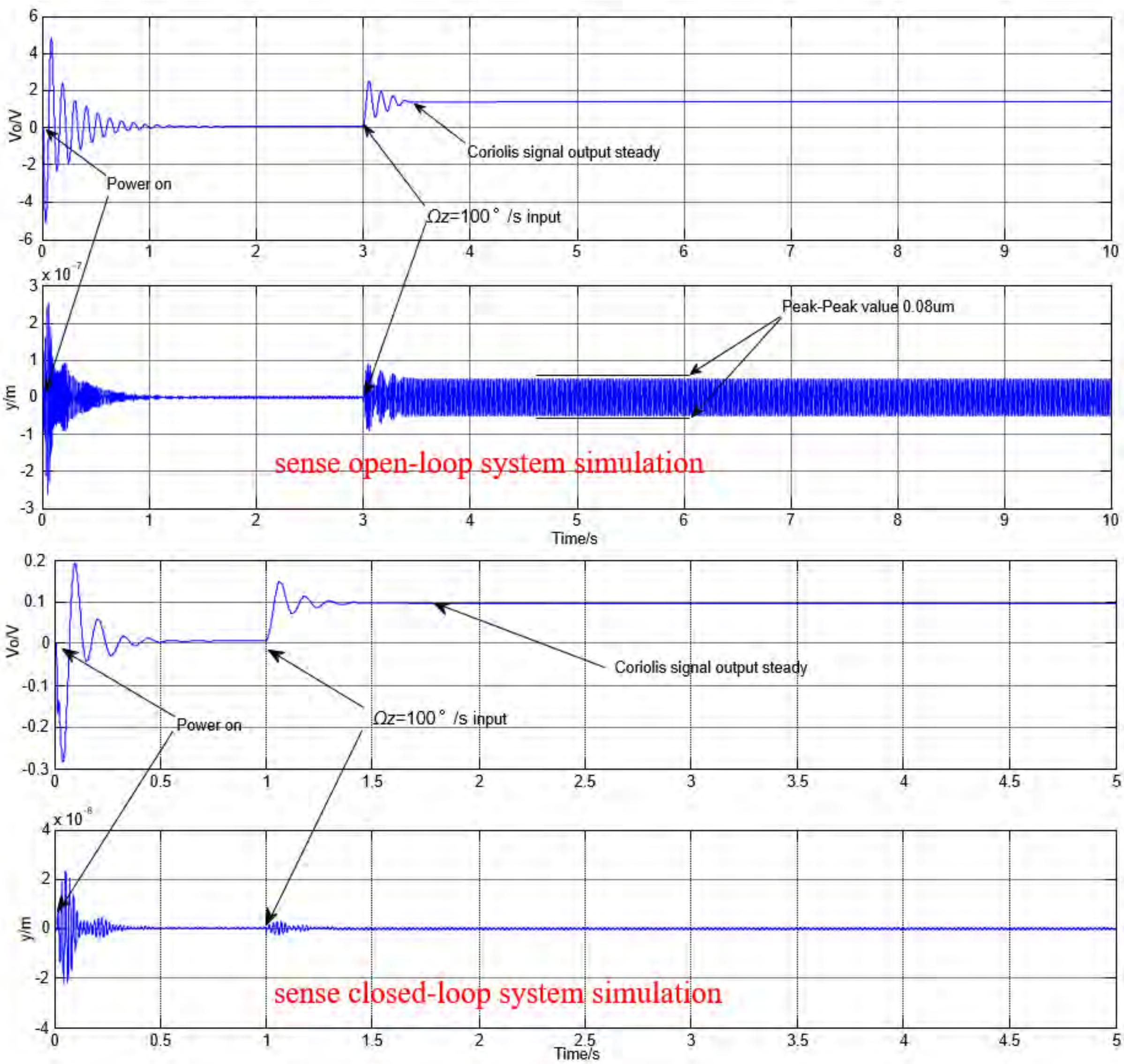


**FIGURE 10.** Sense open-loop and closed-loop system time-domain simulation.

appear in figure 8), the sense channel part (yellow color), and the sense closed-loop controller (BPCTC) part (magenta color). And the "$a_1$, $a_2$, $b_1$, $b_2$" values in figure 9 can be expressed as:

$$F_{\mathrm{BTCPC}} = \frac{R_{12}R_7}{R_{11}R_8}\frac{s^2+a_1s+a_2}{s^2+b_1s+b_2} \tag{19}$$

Their values can be calculated by the parameters in figure 5. Then, the system model is simulated under sense open-loop and sense closed-loop condition, the time-domain simulation results are shown in figure 10.

It can be seen in figure 10, in sense open-loop, the system is "power on" at 0s, and achieve steady state in 1s, after that, the angular rate $\Omega_z = 100$ °/s is applied in the model at 3s, and the Coriolis signal output stays steady at 3.5s. Also, the amplitude of sense mode is about 0.08um (peak-peak value). The simulation results indicate that the sense open-loop system is stable.

In sense closed-loop system in figure 10, the system is powered on at 0s, and the system is steady at 0.5s, then, the $\Omega_z = 100$ °/s is applied in the model at 1s, the system achieves the new steady state at 1.5s. Meanwhile, the sense mode movement amplitude is very tiny, and almost the same as when $\Omega_z = 0$ °/s, this is because the feedback force balanced the Coriolis force generated by $\Omega_z$. The scale factor can be adjusted in $F_{LPFf}$.

The sense closed loop frequency-domain simulation results under different temperatures are shown in figure 11, and the bandwidth (−3dB cut off frequency) is more than 60Hz, which satisfies the design rules (>50Hz). The system stability is verified by "zero-pole" map and "Nyquist" diagrams

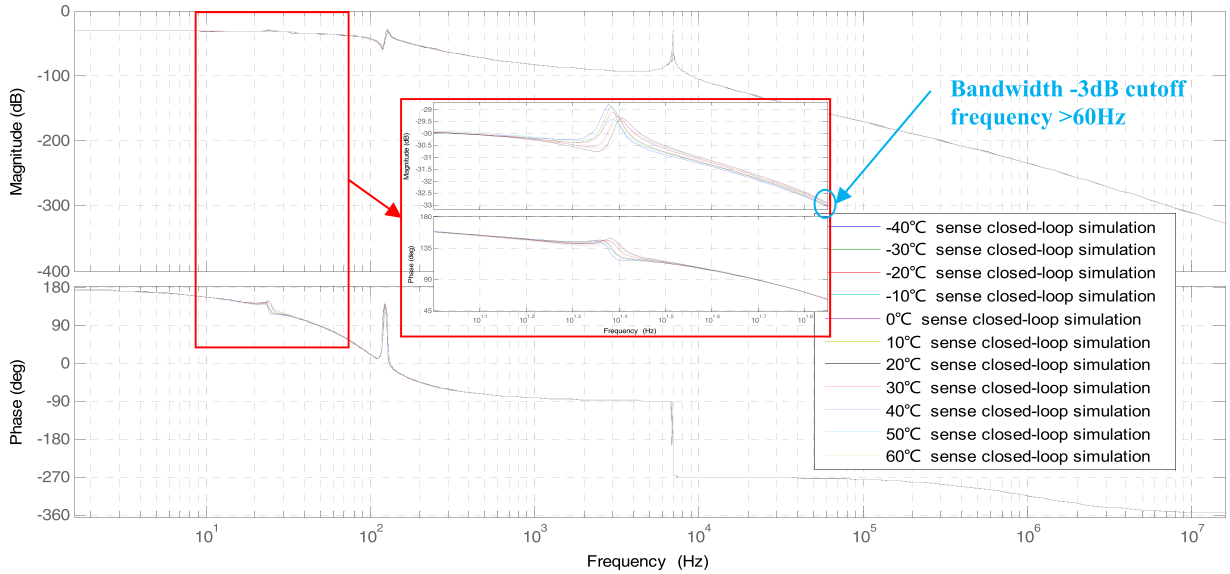


**FIGURE 11.** Sense closed loop system bode map and bandwidth simulation.

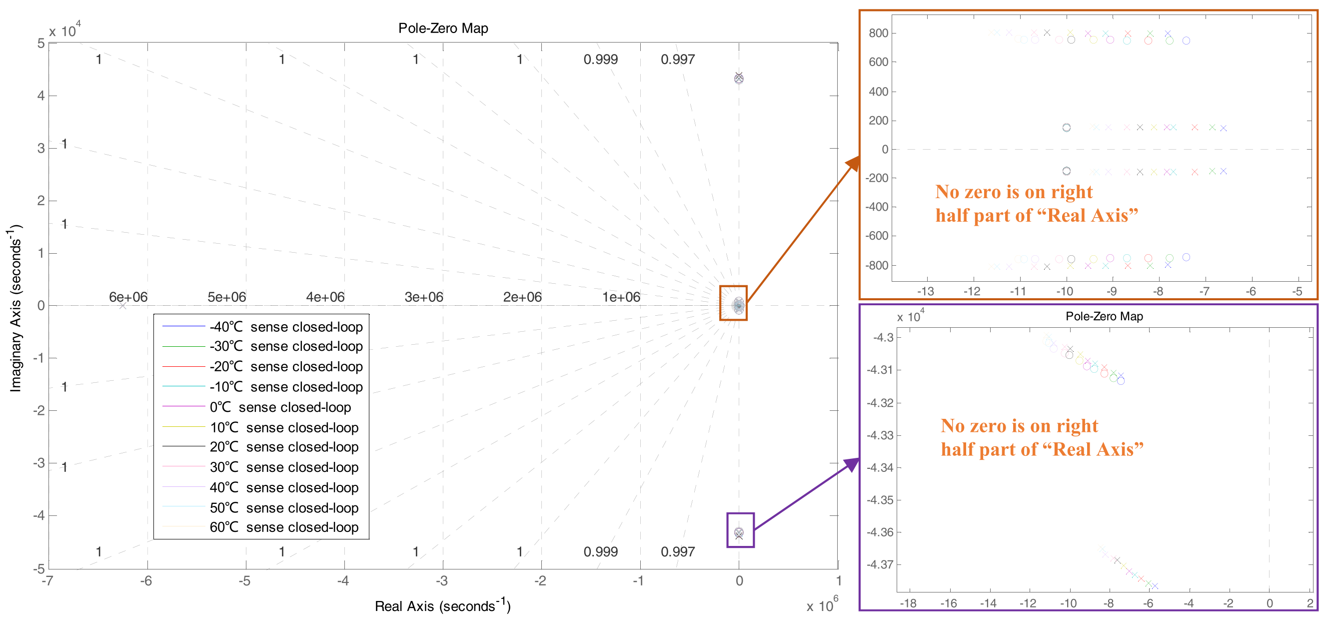


**FIGURE 12.** Sense closed-loop zero-pole map.

which are shown in figure 12 and figure 13. From figure 12, there are not any zero on right part of Real Axis when temperature moves from −40°C to 60°C, which indicates that the system is stable during the full temperature range. Also, the Nyquist diagrams under different temperatures show that the curves did not contains (−1, 0j) point, which verify the system is stable during the temperature range −40°C to 60°C.

So, from the time-domain and frequency-domain simulation, the results show that the sense closed-loop system is rapid and stable, also satisfy the bandwidth design requirement. Then, the system is tested.

## IV. EXPERIMENT

### A. EXPERIMENT PLATFORM AND EQUIPMENT

The gyroscope utilized in the experiments is designed, fabricated by the research group, and the equipment are shown in figure 14. The experiment is on a turntable inside temperature oven (the temperature range covers −40°C to 60°C). The gyroscope structure is packaged in a vacuum ceramic cartridge (quality factors are over 1000, and the test results are shown in figure 6). The monitoring circuit is arranged in three PCBs:

PCB I contains the drive loop part (figure 9 cyan color part) and pre-amplifiers (part ① - ⑪ in figure 8), and connects the

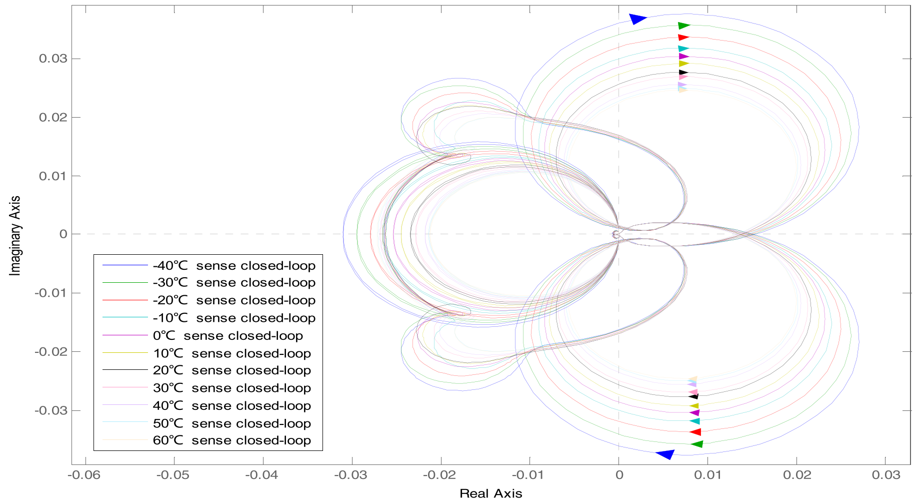


**FIGURE 13.** Sense closed-loop Nyquist diagram.

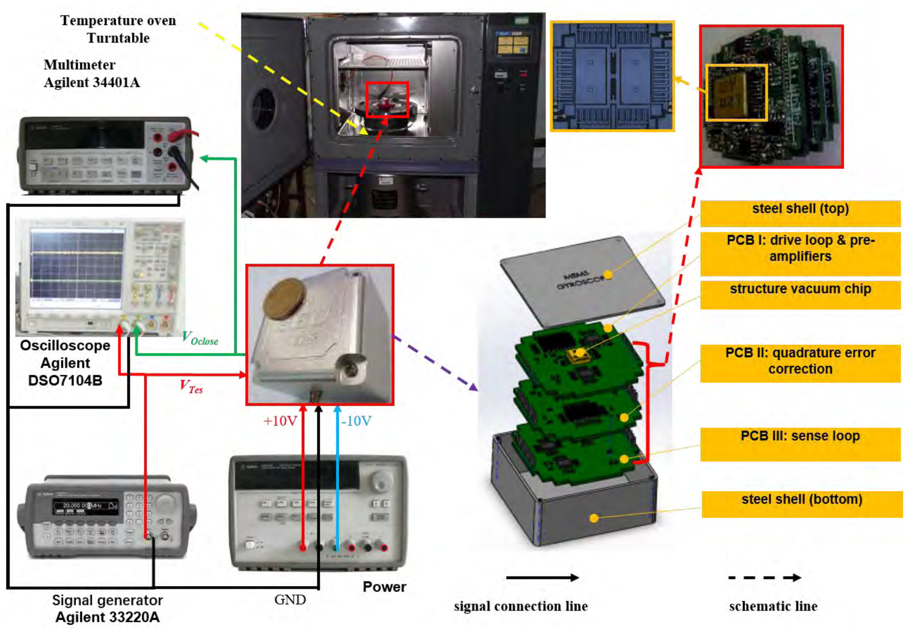


**FIGURE 14.** The MEMS gyroscope test platform.

structure chip. This PCB is carefully designed and dealing with weak signal.

PCB II contains quadrature error correction part (which is shown in figure 9 green color part).

PCB III contains sense loop and contains ⑫-⑳ parts in figure 8. And this PCB can work under both sense open-loop and sense closed-loop conditions. BPCTC part is in this part.

The gyroscope structure chip and the PCBs are packaged in a steel shell, which is connected with "GND" signal, and provides electromagnetism shield. The PCBs are covered with rubber pad, which can protect the system from shock and vibration.

Signals phases and amplitudes are observed with oscilloscope (Agilent DSO7104B), and the data is picked up by multimeter (Agilent 34401A). The power (Agilent E3631A) provides ±10V DC voltage and GND, the signal generator (Agilent 33220A) producing $V_{Tes}$. The temperature oven providing wide-temperature range environment and the bandwidth of the gyroscope is tested by turntable.

### B. MEMS GYROSCOPE SENSE CLOSED-LOOP STATIC TEST

The static experiment follows five steps:

1. Set the environment: release the turntable, and make temperature in oven is set as room temperature, and the sample rate is set as 1Hz.

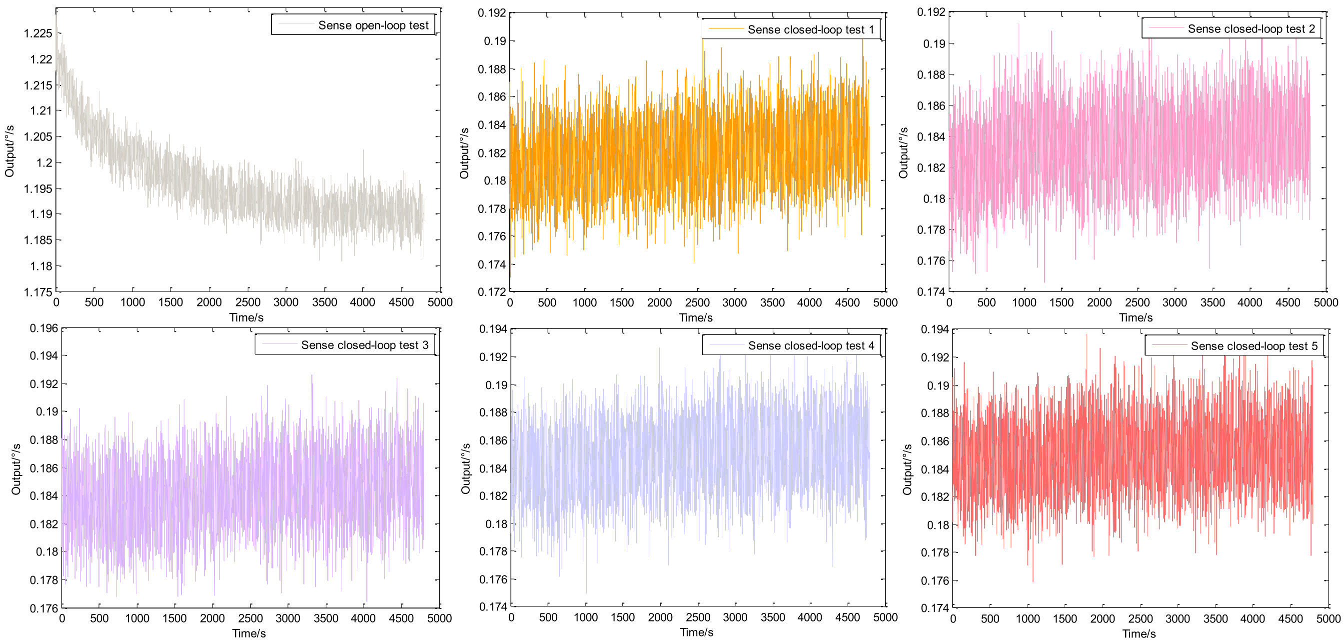


**FIGURE 15.** Sense open-loop and closed-loop static test curves.

2. Pick up the sense open-loop output data: release the turntable, make system works with sense open-loop condition, and power on, pick up the output signal of gyroscope for 4800 seconds.
3. Calculate the sense open-loop scale factor: let the turn table generate $\Omega z = \pm 100°/s$, and collect the gyroscope output values, then calculate the sense open-loop scale factor. Then, draw the output curve of sense open-loop as shown in figure 15.
4. Pick up the sense closed-loop output data: release the turn table, and make system works with sense closed-loop condition, let the system power off for one hour to make sure the system is cool. Then, power on, pick up the output signal of gyroscope for 4800 seconds. Repeat the step 4 for five times to verify the repeatability of the gyroscope.
5. Calculate the sense closed-loop scale factor: let the turn table generate $\Omega z = \pm 100$ °/s, and collect the gyroscope output values, then calculate the sense closed-loop scale factor. Then, draw the output curve of sense closed-loop as shown in figure 15.

From figure 15, it can be seen that, the drift trend is almost eliminated after the sense loop is closed, and the bias value is improved with the help of BPCTC. The five repeatability test for sense closed-loop verify the good repeatability of the sense closed loop.

The Allan derivation results are shown in figure 16, and the bias stability of sense open-loop and sense closed-loop five repeat tests are 2.168 °/h and 0.481 °/h, 0.752 °/h, 0.505 °/h, 0.426 °/h, 0.495 °/h respectively. The angular random walking values of sense open-loop and sense closed-loop five tests are 0.155 $°/\sqrt{h}$ and 0.140 $°/\sqrt{h}$, 0.141 $°/\sqrt{h}$, 0.141 $°/\sqrt{h}$, 0.138 $°/\sqrt{h}$, 0.144 $°/\sqrt{h}$ respectively. The results show that the bias stability performance is improved obviously after the BPCTC sense closed-loop is employed, and the noise characteristic does not been improved significantly. So, BPCTC method can balance the movement caused by Coriolis force, but from equation (14), it can be seen that the BPCTC method is an enhance edition of sense open-loop, which does not influence the noise characteristic very much.

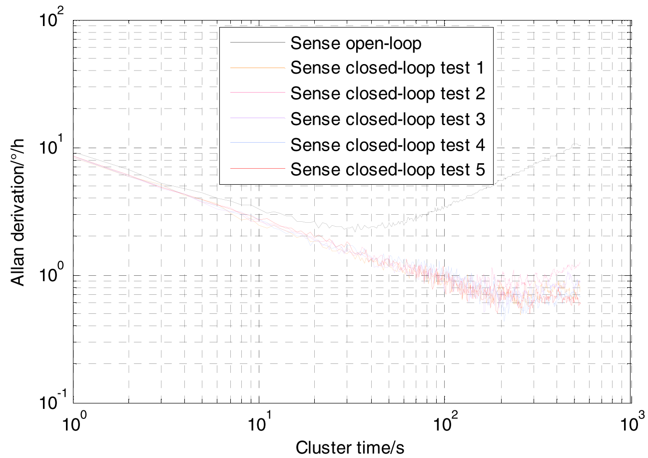


**FIGURE 16.** Allan derivation curves of static test.

### C. MEMS GYROSCOPE SENSE CLOSED-LOOP TEMPERATURE TEST

The temperature experiment follows three steps:

1. Set the environment: release the turntable ($\Omega_z = 0$ °/s), and make temperature in oven go up to 60 °C, and stay one hour to make sure the gyroscope inside temperature is 60 °C.

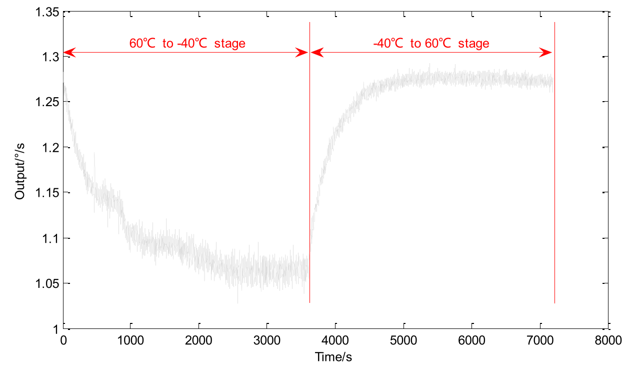


**FIGURE 17.** MEMS gyroscope sense open-loop temperature test.

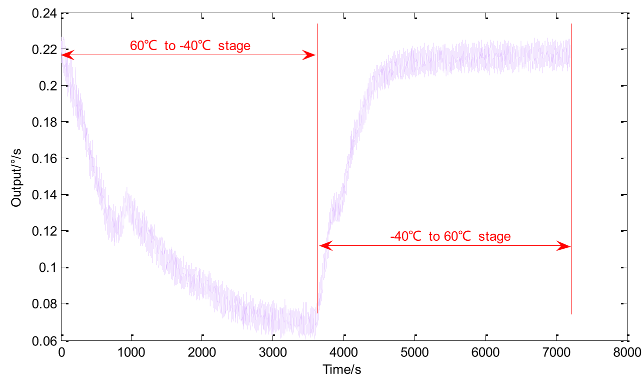


**FIGURE 18.** MEMS gyroscope sense closed-loop temperature test.

2. Pick up the sense open-loop output data: make system works with sense open-loop condition, make temperature down to −40 °C with its max rate. Then, power on, pick up the output signal of gyroscope for 3600 seconds. After that, the temperature inside gyroscope is −40 °C steady, and let temperature go up to 60 °C, also pick up the output data for 3600 seconds (with sampling rate is 1Hz). The curve is shown in figure 17.
3. Pick up the sense closed-loop output data: make system works with sense closed-loop condition, make temperature down to −40 °C with its maximum rate. Then, power on, pick up the output signal of gyroscope for 3600 seconds. After that, the temperature inside gyroscope is −40 °C steady, and let temperature go up to 60 °C, also pick up the output data for 3600 seconds (with 1Hz sampling rate). The curve is shown in figure 18.

In figure 17 and figure 18, it can be seen that the open and closed loop have same temperature trend, and even have same "inflection point" about when time is 900 second. And the temperature coefficient of sense open and closed-loop are calculated by following the equation:

$$B_t = \frac{B_{\max} - B_{\min}}{(60°C-(-40°C))} * 3600 \quad (\circ/h/°C) \qquad (20)$$

where $B_{max}$ and $B_{min}$ are the maximum and minimum value of the output bias during the full temperature range. And from figure 17 and figure 18, it can be calculated that the bias temperature coefficients of sense open-loop and closed-loop are 9.534 °/h/°C and 5.991 °/h/°C respectively.

The bandwidth values of sense open-loop and closed-loop are tested by turntable, and the results show that the sense open-loop and closed-loop bandwidths are 13 Hz and 61Hz.

**TABLE 1.** Gyroscope test conclusion.

| Parameter | Open-loop | Closed-loop |
|---|---|---|
| Bias stability (°/h) | 2.168 | 0.481<br>0.752<br>0.505<br>0.426<br>0.495 |
| Angular random walk (°/√h) | 0.155 | 0.140<br>0.141<br>0.141<br>0.138<br>0.144 |
| Bias temperature coefficient (°/h/°C) | 9.534 | 5.991 |
| Bandwidth (Hz) | 13 | 61 |

## V. CONCLUSION AND DISCUSSION

A novel sense closed-loop for dual-mass gyroscope is proposed in this paper based on bipole temperature compensation proportional controller (BTCPC). The BTCPC is designed by following five rules: compensating undesirable structure mechanical poles, enough bandwidth, gain adjustable, zeros changing with temperature and high frequency noise depression. The BTCPC circuit and system module are simulated, and the gyroscope system model (containing gyroscope structure, drive loop, quadrature error correction loop and sense loop) is established in Simulink Soft and simulated both in time-domain and frequency-domain. The simulation results show that the sense closed-loop system works well and has better speed-ability and stability than open-loop. The monitoring circuit system is realized on three PCBs and the experiments are arranged on static performance, temperature characteristic and bandwidth. The test results show that the bias stability of sense open-loop and sense closed-loop five tests are 2.168 °/h and 0.481 °/h, 0.752 °/h, 0.505 °/h, 0.426 °/h, 0.495 °/h respectively (improves 75.47%). And the angular random walking values of sense open-loop and sense closed-loop five tests are 0.155 °/$\sqrt{h}$ and 0.140 °/$\sqrt{h}$, 0.141 °/$\sqrt{h}$, 0.141 °/$\sqrt{h}$, 0.138 °/$\sqrt{h}$, 0.144 °/$\sqrt{h}$ respectively (improves 9.16%). The temperature experiment result shows that bias temperature coefficients of sense open-loop and closed-loop are 9.534 °/h/°C and 5.991 °/h/°C respectively (improves 37.16%). The bandwidth improves from 13Hz (sense open-loop) to 61Hz (sense closed-loop). The experimental results verify the theoretical analysis and simulation results.

## REFERENCES

[1] K. Tao *et al.*, "Investigation of multimodal electret-based MEMS energy harvester with impact-induced nonlinearity," *J. Microelectromech. Syst.*, vol. 27, no. 2, pp. 276–288, Apr. 2018.

[2] Y. Xu, G. Tian, and X. Chen, "Enhancing INS/UWB integrated position estimation using federated EFIR filtering," *IEEE Access*, vol. 6, pp. 64461–64469, 2018.
[3] H. Cao *et al.*, "Design, fabrication and experiment of double U-beam MEMS vibration ring gyroscope," *Micromachines*, vol. 10, no. 3, p. 186, 2019.
[4] Q. Shen, H. Chang, Y. Wu, and J. Xie, "Turn-on bias behavior prediction for micromachined coriolis vibratory gyroscopes," *Measurement*, vol. 131, pp. 380–393, Jan. 2019.
[5] X. Ding, K. Zhu, and H. Li, "A switch-bridge-based readout circuit for differential capacitance measurement in MEMS resonators," *IEEE Sensors J.*, vol. 17, no. 21, pp. 6978–6985, Nov. 2017.
[6] H. Cao, H. Li, J. Liu, Y. Shi, J. Tang, and C. Shen, "An improved interface and noise analysis of a turning fork microgyroscope structure," *Mech. Syst. Signal Process.*, vols. 70–71, pp. 1208–1220, Mar. 2016. doi: 10.1016/j.ymssp.2015.08.002.
[7] S. A. Zotov, B. R. Simon, I. P. Prikhodko, A. A. Trusov, and A. M. Shkel, "Quality factor maximization through dynamic balancing of tuning fork resonator," *IEEE Sensors J.*, vol. 14, no. 8, pp. 2706–2714, Aug. 2014.
[8] J. Xie, L. Chen, H. Xie, J. Zhou, and G. Liu, "The application of chemical foaming method in the fabrication of micro glass hemisphere resonator," *Micromachines*, vol. 9, no. 42, pp. 1–11, 2018.
[9] H. Cao *et al.*, "Sensing mode coupling analysis for dual-mass MEMS gyroscope and bandwidth expansion within wide-temperature range," *Mech. Syst. Signal Process.*, vol. 98, pp. 448–464, Jan. 2018.
[10] H. Cao *et al.*, "Pole-zero-temperature compensation circuit design and experiment for dual-mass MEMS gyroscope bandwidth expansion," *IEEE/ASME Trans. Mechatronics*, to be published. doi: 10.1109/TMECH.2019.2898098.
[11] C. Shen *et al.*, "Temperature drift modeling of MEMS gyroscope based on genetic-Elman neural network," *Mech. Syst. Signal Process.*, vols. 72–73, pp. 897–905, May 2016.
[12] H. Cao, Y. Zhang, C. Shen, Y. Liu, and X. Wang, "Temperature energy influence compensation for MEMS vibration gyroscope based on RBF NN-GA-KF method," *Shock Vib.*, vol. 2018, Oct. 2018, Art. no. 2830686.
[13] C. Shen, J. Yang, J. Tang, J. Liu, and H. Cao, "Note: Parallel processing algorithm of temperature and noise error for micro-electro-mechanical system gyroscope based on variational mode decomposition and augmented nonlinear differentiator," *Rev. Sci. Instrum.*, vol. 89, Jul. 2018, Art. no. 076107.
[14] H. Cao *et al.*, "Optimization and experimentation of dual-mass MEMS gyroscope quadrature error correction methods," *Sensors*, vol. 16, no. 1, p. 71, 2016.
[15] W.-T. Sung, S. Sung, J. G. Lee, and T. Kang, "Design and performance test of a MEMS vibratory gyroscope with a novel AGC force rebalance control," *J. Micromech. Microeng.*, vol. 17, no. 10, pp. 1939–1948, Oct. 2007.
[16] D. Maeda *et al.*, "MEMS gyroscope with Less than 1-deg/h bias instability variation in temperature range from -40° to 125 °C," *IEEE Sensors J.*, vol. 18, no. 3, pp. 1006–1015, Dec. 2018.
[17] J. Cui, Z. Guo, Q. Zhao, Z. Yang, Y. Hao, and G. Yan, "Force rebalance controller synthesis for a micromachined vibratory gyroscope based on sensitivity margin specifications," *J. Microelectromech. Syst.*, vol. 20, no. 6, pp. 1382–1394, Dec. 2011.
[18] J. Su, D. Xiao, Z. Chen, Z. Hou, and X. Wu, "Dynamic force balancing for the sense mode of a silicon microgyroscope," *Meas. Sci. Technol.*, vol. 24, no. 9, 2013, Art. no. 095105.
[19] C. He, Q. Zhao, Y. Liu, Z. Yang, and G. Yan, "Closed loop control design for the sense mode of micromachined vibratory gyroscopes," *Sci. China Tech. Sci.*, vol. 56, no. 5, pp. 1112–1118, May 2013.
[20] B. Wilcock and M. Kraft, "Genetic algorithm for the design of electromechanical sigma delta modulator MEMS sensors," *Sensors*, vol. 11, no. 10, pp. 9217–9232, 2011.
[21] C. D. Ezekwe and B. E. Boser, "A mode-matching $\Sigma\Delta$ closed-loop vibratory gyroscope readout interface with a $0.004°/s\sqrt{Hz}$ noise floor over a 50Hz band," *IEEE J. Solid-State Circuits*, vol. 43, no. 12, pp. 3039–3048, Dec. 2008.
[22] F. Chen, W. Yuan, H. Chang, G. Yuan, J. Xie, and M. Kraft, "Design and implementation of an optimized double closed-loop control system for MEMS vibratory gyroscope," *IEEE Sensors J.*, vol. 14, no. 1, pp. 184–196, Jan. 2014.
[23] M. Pishrobat and J. Keighobadi, "Force-balancing model predictive control of MEMS vibratory gyroscope sensor," *Proc. Inst. Mech. Eng., C, J. Mech. Eng. Sci.*, vol. 230, no. 17, pp. 1–11, 2015. doi: 10.1177/0954406215607899.
[24] C. H. He *et al.*, "A novel narrow-band force rebalance control method for the sense mode of MEMS vibratory gyroscopes," *Measurement*, vol. 62, pp. 197–204, Feb. 2015.
[25] C. H. He *et al.*, "A novel robust design method for the sense mode of a MEMS vibratory gyroscope based on fuzzy reliability and Taguchi design," *Sci. China Technol. Sci.*, vol. 60, no. 2, pp. 317–324, 2017.
[26] Z. Hu and B. Gallacher, "A mode-matched force-rebalance control for a MEMS vibratory gyroscope," *Sens. Actuators A, Phys.*, vol. 273, pp. 1–11, Apr. 2018.
[27] Z. Deyhim, Z. Yousefi, H. B. Ghavifekr, and E. N. Aghdam, "A high sensitive and robust controllable MEMS gyroscope with inherently linear control force using a high performance 2-DOF oscillator," *Microsyst. Technol.*, vol. 21, no. 1, pp. 227–237, 2015.

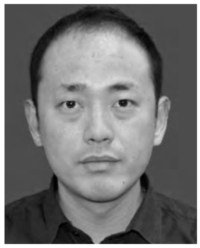

**HUILIANG CAO** (M'18) received the Ph.D. degree in instrument science and technology from Southeast University, Nanjing, China, in 2014. From 2011 to 2012, he was a Research Ph.D. Student with the School of Electrical and Computer Engineering, Georgia Institute of Technology, Atlanta, GA, USA. He is one of the Top Young Academic Leaders of Higher Learning Institutions of Shanxi and Young Academic Leaders of the North University of China. He is currently a Postgraduate Tutor and an Associate Professor with the School of Instrument and Electronics, North University of China, Taiyuan, China. His research interest includes the areas of MEMS inertial devices.

**YU LIU** received the B.S. degree from the North University of China, Taiyuan, Shanxi, China, in 2018, where she is currently pursuing the M.S. degree with the School of Instrument and Electronics. Her research interest includes MEMS gyroscope circuit design.

**YINGJIE ZHANG** received the B.S. degree from the North University of China, Taiyuan, Shanxi, China, in 2017, where he is currently pursuing the M.S. degree with the School of Instrument and Electronics. His research interest includes MEMS sensor structure design.

**XINGLING SHAO** received the M.S. degree in instrument science and technology from the North University of China, Shanxi, China, in 2012, and the Ph.D. degree in navigation, guidance, and control from Beihang University, Beijing, China, in 2016. Since 2016, he has been with the Department of Instrument and Electronics, North University of China, as a Professor. His current research interests include anti-disturbance control theory and application for nonlinear uncertain systems.

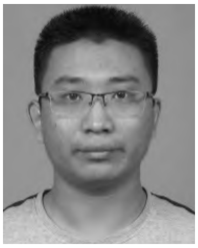

**JINYANG GAO** received the B.S. degree from the University of Electronic Science and Technology of China, Sichuan, China, in 2012, and the Ph.D. degree from Shanghai Jiaotong University, Shanghai, China, in 2017. He is currently an Assistant Professor with the North University of China, Shanxi, China. His research interests include capsule robot, wireless power transmission and related electronic circuit design, and gastrointestinal biomechanics.

**KUN HUANG** received the B.S. and M.S. degrees from the North University of China, Shanxi, China, in 2008 and 2011, respectively, and the Ph.D. degree from Shanghai Jiao Tong University, in 2016. He has been with the North University of China, since 2016. His research interest includes the semiconductor micro-nano electromechanical device in the systems.

**YUNBO SHI** received the B.S. and M.S. degrees from the North University of China, Shanxi, China, in 1995 and 2003, respectively, and the Ph.D. degree from the Beijing Institute of Technology of China, in 2014. He is currently a Professor with the North University of China. His research interest includes measurement and semiconductor materials and devices.

**JUN TANG** received the B.S. and M.S. degrees from the North University of China, Taiyuan, China, in 2003 and 2006, respectively, and the Ph.D. degree from the National Technical University of Athens, Athens, Greece, in 2010. He has been a Professor with the North University of China, since 2016. His research interests include micro electromechanical system inertial sensor and nano phase materials.

**CHONG SHEN** received the Ph.D. degree in instrument science and technology from Southeast University, Nanjing, China, in 2013. He is currently an Associate Professor with the School of Instrument and Electronics, North University of China, Taiyuan, Shanxi, China. His research interests include MEMS inertial devices de-noising and inertial guidance system design.

**JUN LIU** received the Ph.D. degree from the Beijing Institute of Technology, Beijing, China, in 2001. From 2001 to 2005, he was a Postdoctoral Researcher with Peking University. He is currently a Distinguished Professor with the North University of China, Taiyuan, China. His current research interests include intelligent instrument, micro inertia devices, and micro electromechanical system devices.